Structural characterization of ZrO_2 nanoparticles obtained by aerosol pyrolysis

M. Vallet-Regí,[a] S. Nicolopoulos,*[a] J. Román,[a] J. L. Martínez[a] and J. M. González-Calbet[b]

[a]*Departamento Química Inorgánica y Bioinorgánica, Facultad Farmacia, Universidad Complutense, 28040 Madrid, Spain*

[b]*Departamento Química Inorgánica, Facultad Químicas, Universidad Complutense, 28040 Madrid, Spain*

Fine zirconium oxide powders have been obtained by pyrolysis of an aerosol produced by ultrahigh frequency from a zirconium oxalate solution. The as-received material, obtained at 400 °C, is amorphous and constituted of hollow spherical particles. This material was annealed under different conditions producing nanometric particles of ZrO_2. A study of the equilibrium between the monoclinic and the cubic/tetragonal phase as a function of the thermal treatment has been performed. Crystallographic characterization of the fine zirconia particles obtained has been accomplished using electron diffraction and high-resolution electron microscopy, revealing that even individual nanometric ZrO_2 particles could contain multiple twin variants.

Zirconium oxide (ZrO_2) is a material which has been widely investigated in recent years, either in the pure state[1,2] or mixed with other oxides,[3,4] for its applications in high-technology materials. An important characteristic of ZrO_2 is the existence of various polymorphic forms depending on temperature.[5] Three different crystalline forms can exist, namely monoclinic (M-ZrO_2) ($a=0.5121$ nm, $b=0.5196$ nm, $c=0.5316$ nm, $\beta=98.83°$); tetragonal (T-ZrO_2) ($a=0.3632$ nm, $c=0.5075$ nm) and cubic (C-ZrO_2) ($a=0.5128$ nm). Transition temperatures between these phases are not accurately known, but it has been stated that the monoclinic phase is stable up to 1373 K.[6] Around such a temperature ZrO_2 transforms to the tetragonal phase over a range of *ca.* 100 K. Above 2573 K, the stable phase is the cubic form. However, several authors have described the presence of both cubic and tetragonal metastable phases at low temperature.[7,8]

Garvie[9] proposed that the reason for the stability of the tetragonal phase was an effect of the particle size since particles below a critical size of 30 nm are stabilized in this phase independently of the synthetic method. Other authors have, however, attributed the stability of metastable phases to factors such as the pH during gel precipitation,[10] retention of either water or anions,[11,12] or the presence of reticular defects.[10–12] If ZrO_2 is obtained with small particle size and high specific surface, then two important applications of the material are as a bifunctional acid–base catalyst and as a catalyst support in heterogeneous catalysis. For these purposes, it is crucial to prepare materials with high specific surface, an adequate porous texture and, if possible, high resistance to sintering. Several methods have been described to obtain active ZrO_2. The nature of the crystalline phases, the specific surface area and the porosity depend on the synthesis method and on the conditions employed. There are two general preparation pathways; coprecipitation and the sol–gel technique, and for the latter, two different routes can be differentiated depending on whether the precursor is an aqueous solution of an inorganic salt or is a metal–organic compound. Here, we report on the pyrolysis of an aerosol as an alternative method to produce small particles which are useful in catalytic applications.

Another interesting fact to point out is that the reversible T-ZrO_2–M-ZrO_2 transition is martensitic, as for induced plasticity (TRIP) steels.[13,14] The transformation of T-ZrO_2 into M-ZrO_2 has been used to enhance the toughness of matrix materials.[15,16] In order to control the degradation of electrical and mechanical properties of tetragonal and cubic zirconia it is necessary to prevent the T-ZrO_2–M-ZrO_2 transformation by the addition of the appropriate dopants[17] (*e.g.* Y_2O_3, CeO_2, CaO) but high-temperature phases can also be prepared, without the addition of stabilizers,[18] by synthesizing the ZrO_2-C/T phase with small particle size. On the other hand, in ceramic composites containing zirconia or in glass-ceramics containing zirconia, the grain size is a critical factor for the T-ZrO_2–M-ZrO_2 transformation. Therefore, although the mechanism of tetragonal phase stability is still not clear it seems that the correlation microstructure–temperature of the T-ZrO_2–M-ZrO_2 transition depends on the particle size.[19] Moreover, the preparation conditions may have a significant influence on the size of zirconia nanoparticles thus playing an important role in the physical properties of the material. It has been demonstrated[20] that HREM imaging allows the study of structural changes accompanying phase transformations (*e.g.* internal twinning) which occur in such nanoparticles. Here, we show that, by using appropriate characterization techniques, such as X-ray diffraction (XRD) and, especially, high-resolution electron microscopy (HREM), we can study the microstructural characteristics of ultrafine zirconia particles obtained by pyrolysis of an aerosol treated under different annealing conditions.

Experimental

Particle preparation

Reagent grade zirconium tetrachloride (Fluka) and oxalic acid dihydrate (Merck) were used as-received; 23.3 g of $ZrCl_4$ were dissolved in 300 ml of distilled water. Aqueous ammonia (25%, Fluka) was added to this solution until complete precipitation occurred. The precipitate was separated by centrifugation and then dissolved in 0.4 M oxalic acid solution with continuous stirring and heating at 60 °C. When the solid had dissolved, the solution was diluted to 1 l with distilled water. Fine particles of ZrO_2 were obtained by pyrolysis of the aerosol generated by ultrahigh frequency spraying of the solution, using processing equipment previously reported.[21] The process was performed with an air flow of 4.5 l min^{-1}, a furnace temperature of 400 °C and an aerosol flow of 0.5 ml min^{-1}. The *in situ* material was placed in a furnace at 25 °C and the temperature was raised at 10 °C min^{-1} up to 500, 600, 700, 800 and 900 °C. At each temperature, three distinct annealing times were applied (0, 30 or 60 min).

Particle characterization

Powder XRD data were obtained on an X'Pert MPD diffractometer. Measurements were carried out with a step size

of 0.02° (2θ) and 10 s for each step, and clear, sharp diffraction profiles were obtained. Particle morphology was examined by scanning electron microscopy (SEM) on a JEOL 6400 microscope. Thermogravimetric analysis (TG and DTA) was carried out on a Seiko TG–DTA 320, in air, with a heating rate of 20 °C min^{-1} and using pure alumina as reference.

Specimens for HREM observations were obtained as dry dispersions on copper grids covered with holey carbon films. The HREM study was performed with a JEOL 4000EX transmission electron microscope operating at 400 kV and equipped with a top-entry double-tilt goniometer stage. HREM micrographs were recorded at a magnification of 500 000, scanned with an EPSON GT9000 and processed with CRISP software[22] run on a 486/50 MHz Compaq computer. Several diffractograms have been examined from small areas of the digitized micrographs (with diameters as low as 2 nm) by centring on the area of interest.

Calculated diffractograms have been performed with the aid of the 'Ideal Microscope' software.[23] Selected area electron diffraction (SAED) was used to study the crystalline structure of the fine zirconia particles. Conventional electron microscopy observations were obtained with a JEOL 2000FX in a conventional TEM mode operating at 200 kV.

Results and Discussion

Structural studies by XRD

The powder XRD pattern indicates that the as-received sample is amorphous [Fig. 1(*a*)]. The powder XRD pattern of the residue at 900 °C can be indexed on the basis of zirconium oxide. Crystalline phases of the annealed samples were identified by XRD [Fig. 1(*b*), (*c*)]. All samples annealed at 500 °C and that annealed at 600 °C (*in situ*) were found to be amorphous.

The corresponding TG–DTA curves show an endothermic mass loss at 100 °C due to the elimination of adsorbed water (Fig. 2). A second mass loss, also endothermic, in the range 240–360 °C, corresponds to the elimination of coordinated water and internal dehydration. Finally, the mass loss detected at 500–750 °C (exothermic process) is due to the decomposition of organic matter present in the precursor solution.

In the remainder of the samples, powder XRD patterns show the presence either of monoclinic or cubic/tetragonal ZrO_2. The percentage of C/T-ZrO_2 was evaluated by using the equation proposed by Garvie[24] and the results are given in Table 1.

According to XRD analysis, samples prepared at 600 or 700 °C and annealed for 30 or 60 min, respectively, show the presence of 100% C/T-ZrO_2. But, if either the time or temperature are increased, a transition to the monoclinic phase takes place.

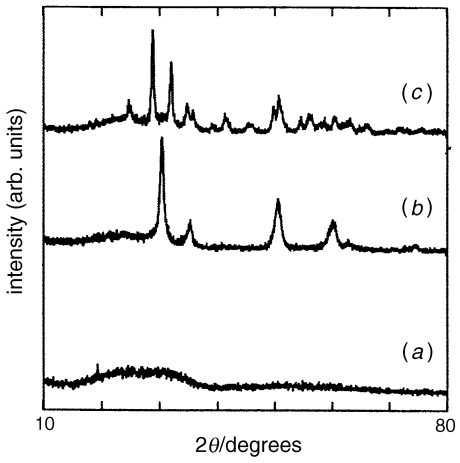

Fig. 1 Powder XRD pattern of (*a*) as-received sample, (*b*) tetragonal phase and (*c*) monoclinic phase

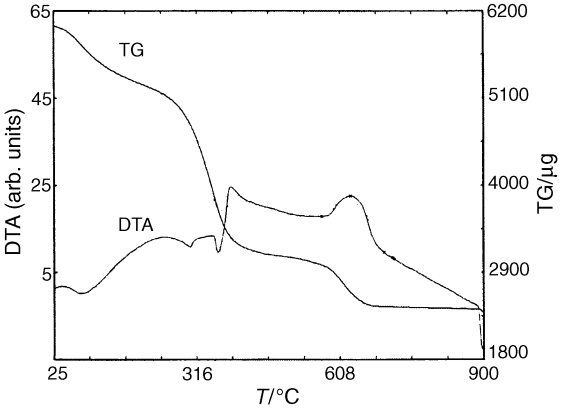

Fig. 2 TG–DTA curves of an as-received pyrosol zirconia sample

Table 1 Percentage of C/T-ZrO_2 in the annealed samples according to XRD analysis (C = cubic; T = tetragonal; M = monoclinic; A = amorphous)

T/°C	0 min	30 min	60 min
500	A	A	A
600	A	100 C/T	92 C/T + 8 M
700	100 C/T	94 C/T + 6 M	84 C/T + 16 M
800	94 C/T + 6 M	60 C/T + 40 M	39 C/T + 61 M
900	38 C/T + 62 M	6 C/T + 94 M	6 C/T + 94 M

A profile fitting based on a Marquardt non-linear least-squares algorithm[25,26] has been subsequently applied to selected ranges of the data, allowing the elimination of background contributions and the separation of overlapping diffraction maxima. The values of diffraction intensities and full widths at half maximum (FWHM) for the more intense reflections were taken from the fitted profiles. Using as reference a sample annealed at 1000 °C for 72 h for the M-ZrO_2 phase and a sample annealed at 800 °C for 30 min for the C/T-ZrO_2 phase, it is possible to estimate the average crystallite size, by means of the Scherrer equation,

$$\text{Average crystallite size} = (K\lambda/B)\cos\theta \qquad (1)$$

where K is a shape factor value,[27] λ is the wavelength and B is the difference in FWHM between broadened and standard maxima. Such a broadening is attributed only to the crystallite size, neglecting lattice distortion contributions. Evolution of C/T and M-ZrO_2 particle size (in nm) upon thermal treatment is shown in Table 2.

In both cases (C/T-ZrO_2 or M-ZrO_2) the grain size increases with increasing annealing temperature and for a given temperature, the grain size increases with annealing time.

In order to determine the morphology of the particles an SEM study was performed. It can be seen [Fig. 3(a)] that the as-received sample consists of thin smooth-walled hollow spherical particles with diameters between 0.5 and 3 μm. The annealed samples [Fig. 3(b)] are also hollow spherical particles of the same average size but an increase of the thickness is observed with the surface being granular. This is due to loss

Table 2 Average grain size (nm) for C/T and M-ZrO_2

T/°C	0 min	30 min	60 min
500	—	—	—
600	—	12.8–15.7	14.3–18.0
700	12.6–19.0	15.2–18.1	19.5–22.3
800	16.6–19.0	19.2–22.9	20.1–25.7
900	25.1–28.0	25.1–28.0	27.2–29.8

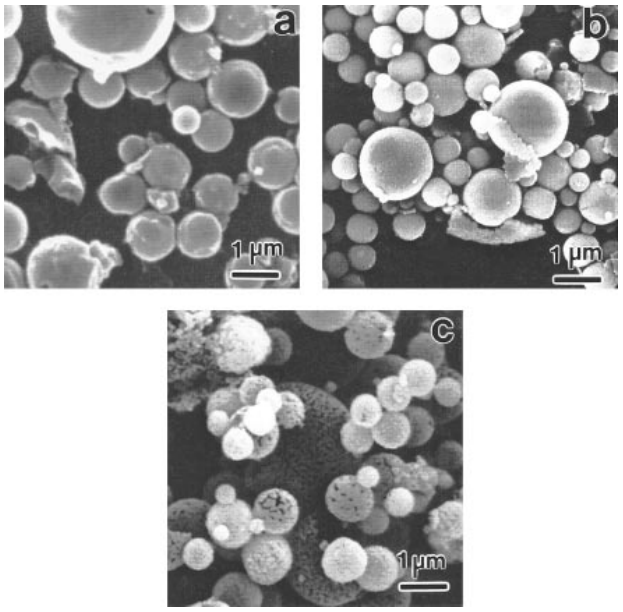

Fig. 3 SEM images showing the morphology of the as-received sample (a), of particles annealed for 30 min at 900 °C (b), and for 78 h at 900 °C (c)

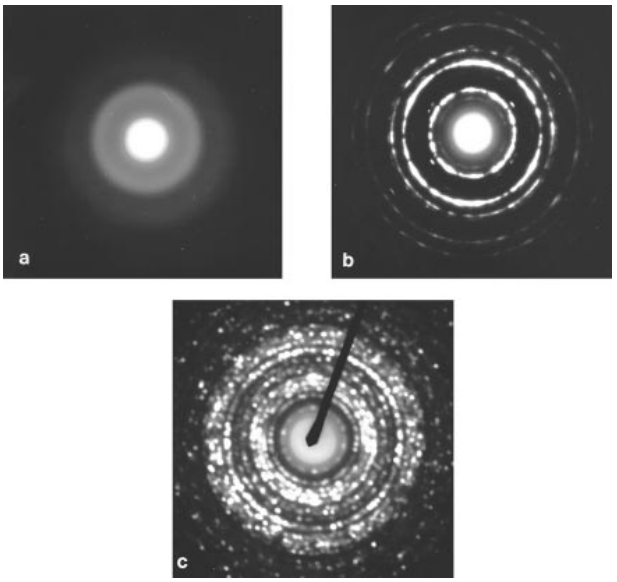

Fig. 5 SAED patterns of the as-received material (a), of a sample annealed for 30 min at 600 °C (polycrystalline rings are consistent with C structure) (b), and of a sample annealed for 60 min at 900 °C (M structure) (c)

of water and the formation of fine zirconia crystallites on the walls of the large spherical particles. Crystal formation is evident when the annealing temperature is higher than 900 °C, as observed in Fig. 3(c).

Structural studies by conventional TEM

Conventional TEM micrographs at low magnification (100 000 ×) of the prepared samples (Table 2) confirm the SEM results, *i.e.*, the average diameter of the hollow pyrosol spherical particles is between 0.5 and 3 μm. On the other hand, fine zirconia particles are formed on the surface, the size of which increased with temperature and/or annealing time (Fig. 4).

TEM observations allow direct imaging of the zirconia particle size. Table 3 shows size variation of the fine zirconia particles as a function of the annealing conditions. Samples annealed at 500 °C do not reveal any fine particle structure in the walls of the pyrosol spheres.

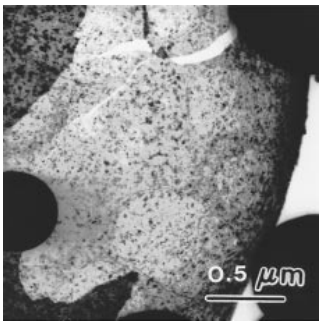

Fig. 4 Low-resolution TEM image of pyrosol spherical particles (sample prepared at 600 °C, 30 min). Several fine zirconia crystallites are seen on the surface.

As seen in Table 3 (and in agreement with the XRD analysis), the particle size increases at higher annealing temperatures. The estimated particle sizes appear larger by TEM than estimated by XRD diffraction.

Such a discrepancy can be explained on the basis that measured particle size according to XRD refers only to coherent domains. Fine zirconia particles observed by TEM could be polydomain in nature (*e.g.*, constituted by two or more twin-related particles). This will be discussed below, in light of HREM observations.

The crystal structure of synthesized pyrosol particles has also been examined by electron diffraction. Diffraction patterns have been obtained by focusing the beam in to hollow pyrosol spheres; it is generally difficult to perform microdiffraction on individual fine zirconia crystallites as they are usually small (especially at low annealing temperatures) and densely agglomerated on the surfaces of the large hollow spheres (Fig. 4). The results are also presented in Table 3. In all cases the SAED results confirm the XRD data.

The corresponding diffraction pattern of the as-received material [Fig. 5(a)] is formed by poorly defined rings revealing that the sample is not yet crystallized; when the material is crystallized and the size of the fine zirconia particles formed on the surface of the large hollow spheres is small, SAED patterns consist of rings consistent with either the C, T or M-ZrO_2 polycrystalline forms (or mixtures of them) [Fig. 5(b)].

At high temperatures and/or longer annealing times, polycrystalline rings change to spot patterns consistent with the superposition of several individual particles in different crystallographic orientations [see Fig. 5(c)].

Table 3 Size and structural changes of the powder, depending on the preparation conditions (according to TEM and SAED observations)

T/°C	0 min	30 min	60 min
500	—(A)	—(A)	—(A)
600	8–20 nm (C/T)	8–30 (C/T + M[a])	15–30 nm (C/T + M)
700	15–30 nm (C/T + M)	5–40 nm (C/T + M)	15–50 nm (C/T + M)
800	15–50 nm (C/T + M)	15–60 nm (C/T + M)	20–80 nm (C/T + M)
900	15–80 nm (C/T + M)	20–70 nm (C/T + M)	20–90 nm (C/T + M)

[a]Trace.

Structural studies by HREM

As we have seen before, even though conventional TEM studies provide a good characterization of the fine pyrosol crystallites, this technique cannot be used to study the crystal structure of ultrafine individual zirconia crystallites. For example, a still unresolved structural feature of the T-ZrO_2–M-ZrO_2 transition in zirconia concerns twinning, which is commonly observed in monoclinic ZrO_2. Such particles appear to contain twin-related variants or a mixture of hybrid crystals.[28,29] However, it was reported that internal twins or coexisting hybrid crystals of the two phases were absent in fine particles of zirconia.[30] Twinning is believed to occur in bulk materials to accommodate, at least partially, the shape change associated with the T-ZrO_2–M-ZrO_2 transformation.[31–33] In a recent work, fine zirconia particles prepared by a sol–gel technique were found to contain single or multiple twin variants[29] associated with the T-ZrO_2–M-ZrO_2 transition.

In view of the above results it is important to characterize the structural aspects of the fine pyrosol zirconia particles using HREM. According to Table 2, at 600 °C and 30 min annealing time, fine zirconia particles are formed and, probably, under these conditions the T-ZrO_2–M-ZrO_2 transformation begins to occur since some monoclinic traces are observed in the SAED pattern (Table 3). Conventional TEM images show that crystallites of 20–30 nm are inside the pyrosol sphere (see Fig. 4). Nevertheless, under the same preparation conditions, we have observed (although rarely) pyrosol spheres with individual fine crystallites of $\geqslant 50$ nm (Fig. 6). For such crystallites, SAED and subsequent HREM work can be performed on individual particles.

Fig. 7 shows an HREM image of such a zirconia crystallite along with the corresponding SAED pattern. This pattern seems to show four-fold symmetry (with $a = 0.52$ nm) more clearly visible in the thinner part of the crystal. However, careful measurement of the almost square arrangement of bright dots leads to distances 0.52 and 0.51 nm corresponding to d_{010} and d_{100} of the [001] projection of the monoclinic structure. On the other hand, a slight spot splitting in the SAED pattern (see arrows) can be observed indicating the possible existence of twins. Moreover, reflections $(0k0)$ $(k = 2n)$ also appear, although kinematically forbidden (presumably because of strong secondary/dynamical contributions).

In Fig. 8(a), a wider area of the same pyrosol particle is observed. Abrupt changes in symmetry and contrast occur not only at thicker regions of the crystal but also along the thinner edges. This suggests that at least part of the explanation for the apparently anomalous behaviour of the image may arise simply from the breakdown of symmetry arising from elastic bending of the lattice planes (see also ref. 34). Moreover, digital diffractograms from different areas (A, B) in this HREM image

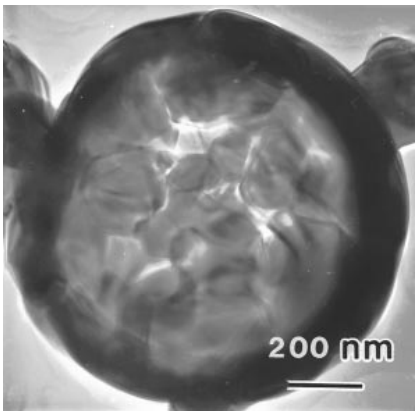

Fig. 6 TEM image of pyrosol hollow spherical particles (sample prepared at 600 °C, 30 min). Fine zirconia particles of 50 nm are observed on the surface of the sphere.

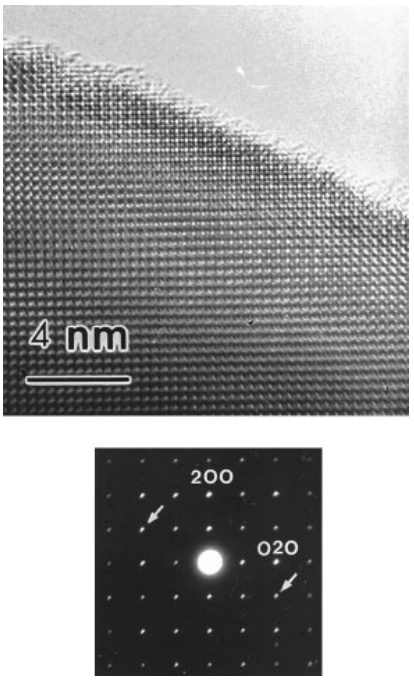

Fig. 7 HREM image of a fine zirconia particle along the $[001]_M$ orientation (top) with its corresponding SAED pattern (bottom); arrows indicate spot splitting

[Fig. 8(b) and (c)] show some spot splitting parallel to distinct directions depending on the diffracting area of the crystallite. The calculated diffraction pattern [Fig. 8(d)] clearly shows extinctions corresponding to this space group.

This configuration is very similar to that observed by van Tendeloo *et al.*[28] in the ZrO_2–ZrN system, where different monoclinic variants having a common c_M axis parallel to the electron beam induce a spot splitting in the SAED pattern parallel to $[110]_M$. The observed spot splitting in the SAED pattern (Fig. 7) is parallel to $[110]_M$ and could be compatible with the existence of (110) twins. The existence of different domains would also induce local contrast and symmetry changes as is indeed observed in the HREM image of Fig. 8, although local crystal bending also induces contrast changes, as we have commented previously.

The point group symmetry decreases during the T-ZrO_2–M-ZrO_2 transformation (from $4/mmm$ to $2/m$) and the order of symmetry decreases from 16 to 4. Consequently, this results in the occurrence of $(16/4 = 4)$ different monoclinic variants while the transformation occurs.[35] These different orientation variants have a common c_M axis (see Fig. 9). Variants 1 and 2 have their b axes parallel while variants 3 and 4 have parallel b-axes, but are perpendicular to those of variants 1 and 2. These four variants, however, only produce two different interfaces.[28]

It is well established that optical diffraction experiments can correctly simulate the geometry of SAED phenomena. In order to simulate the SAED effects due to the existence of the different orientation variants, we have prepared optical masks of the type shown in Fig. 10, containing arrays of 15×15 dots. Two different types of interface in respect to the lattice of points were tested [according to ref. 28, either parallel to $(100)_M$ or parallel to $(110)_M$]. In each case, the direction of splitting was found always to be perpendicular to the interface direction (independently of the type of boundary, *i.e.*, conservative or non-conservative). The above results are in agreement with ref. 36, where it is demonstrated that the direction of spot splitting is always perpendicular to the interface boundary.

When the crystallite of Fig. 8 is tilted around $[010]_M$, another orientation can be observed [see Fig. 11(a)]. In the HREM image a rapid contrast variation is observed towards

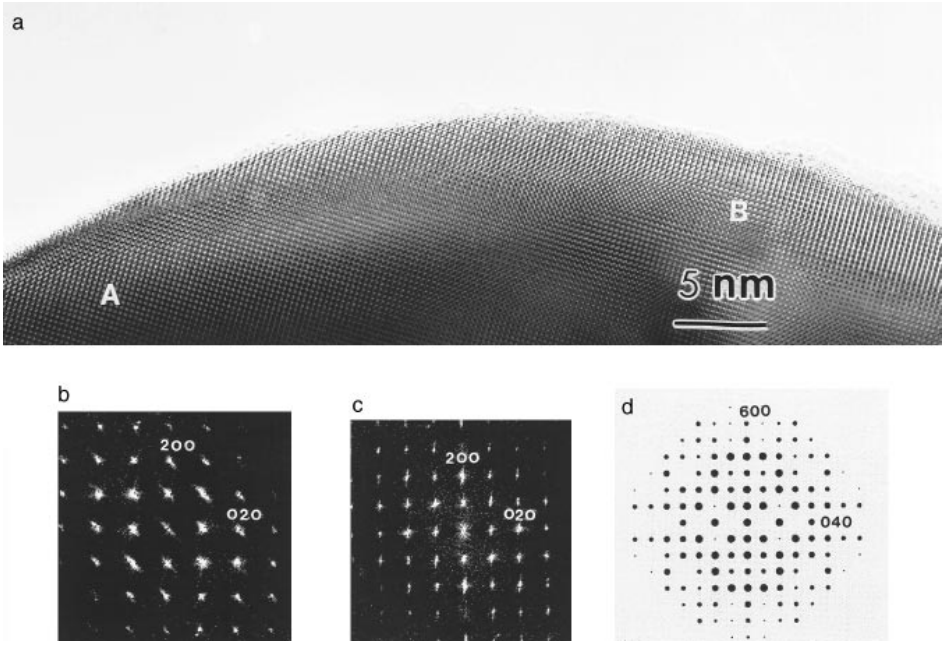

Fig. 8 (a) Wider area of the HREM image of Fig. 7. (b), (c) Digital diffractograms from areas A and B indicate spot splitting along $[110]_M$ and $[100]_M$, respectively. (d) Corresponding $[001]_M$ calculated diffraction pattern.

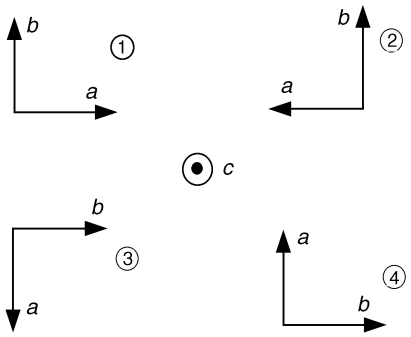

Fig. 9 Schematic representation of four different orientation variants having a common c axis in the twinned monoclinic phase (after ref. 18)

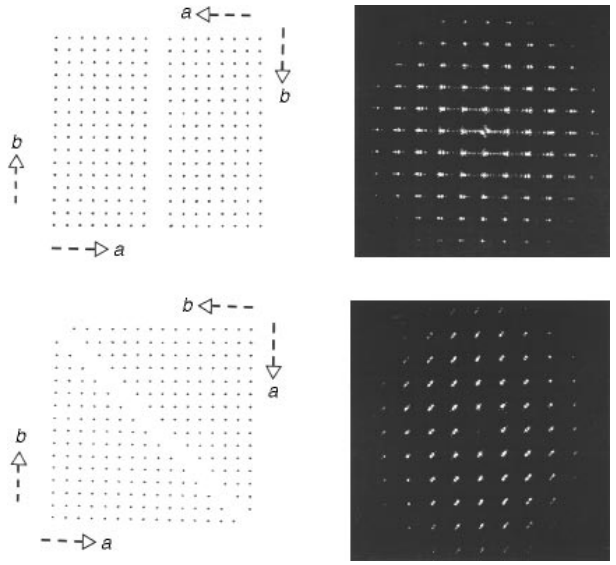

Fig. 10 Two optical masks consisting of 15×15 dot arrays representing different orientational variants (OV) having a common c_M axis and separated by a single interface. Their corresponding diffraction patterns are also shown. Top, OV 1 and 2; bottom, OV 1 and 4. Note that the direction of spot splitting is perpendicular to the interface.

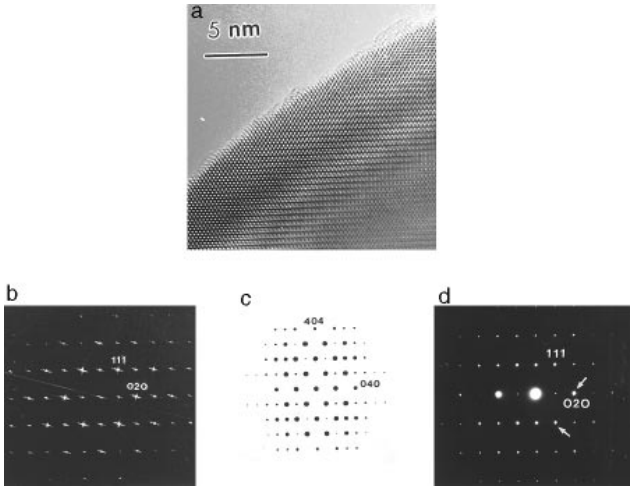

Fig. 11 (a) HREM image of a fine zirconia particle along the $[101]_M$ orientation with its corresponding experimental SAED pattern (b); arrows indicate weak spot splitting. (c) Digital diffractogram of the HREM image again shows spot splitting. (d) Corresponding $[101]_M$ calculated diffraction pattern.

the thicker region of the crystal. The corresponding SAED pattern can only be interpreted on the basis of a monoclinic structure as seen parallel to the [101] direction; the spacing of 0.314 nm observed in the SAED pattern [Fig. 11(b)] is characteristic of the $d_{(111)M}$ structure.

The digital diffractogram performed on the $[101]_M$ HREM image [Fig. 11(c)] shows a clear splitting of the diffraction spots. Such an effect (although very weak) can also be seen in the corresponding SAED pattern. The latter effect could be consistent again with the existence of different orientation domains inside the zirconia crystallite. The calculated diffraction pattern show the extinctions corresponding to this space group [Fig. 11(d)].

In fact, when turning about the $[010]_M$ orientation, some orientational variant (*e.g.*, variant 4 in Fig. 10) is brought in the [101] orientation (Fig. 12). Another variant (*e.g.*, variant 3) is brought near the $[011]_M$ orientation. Overlapping of both patterns may explain the observed weak spot splitting in the SAED pattern. However, one must be cautious with the

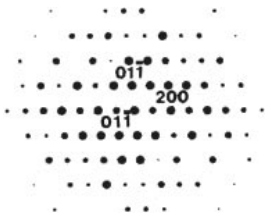

Fig. 12 Calculated SAED pattern for $[011]_M$ monoclinic zirconia

interpretation of the observed spot splitting in the digital diffractogram [Fig. 11(c)] as long as rapid changes in contrast (*e.g.* due to abrupt thickness variations) could probably induce such an effect. The above also holds for the interpretation of the observed spot splitting in digital diffraction patterns of Fig. 8. Therefore, because of the rapid contrast variation due to possible local lattice bending and thickness variation inside the fine zirconia particles, the contrast from different (possible) orientation domains cannot be discerned in a straightforward manner from HREM images. On the other hand, the observed splitting of spots in the SAED patterns of Fig. 8 and 11 is consistent with the existence of different orientation domains inside the zirconia crystallite.

Conclusions

Fine zirconia powders obtained by pyrolysis of an aerosol have been synthesized. Particle sizes, as observed by conventional TEM, appear bigger in comparison to the estimated value given by XRD profile analysis. This could be explained on the basis that for XRD analysis only the size of coherent domains can be estimated; in fact, even fine zirconia particles may contain multiple individuals. The existence of multiple twin domains probably associated with the T-ZrO_2–M-ZrO_2 transition is compatible with the observed spot splitting in the SAED pattern. However, interpretation of HREM images on a basis of different (twin) domains is not straightforward as local lattice bendings and abrupt thickness variations may produce frequent contrast variations.

Financial support by CICYT (Spain) through Research Projects No. MAT96-0919 and MAT95-0624 is acknowledged.

References

1 R. Srinivasan, C. R. Hubbard, O. B. Cavin and B. H. Davis, *Chem. Mater*., 1993, **5**, 27.
2 X. Turillas, P. Barnes and D. Hausermann, *J. Mater. Res*., 1993, **8**, 63.
3 C. M. Foster, G. R. Bai, J. C. Parker and M. N. Ali, *J. Mater. Res*., 1993, **8**, 1977.
4 Y. Ikuma, T. Sugiyama and J. Okano, *J. Mater. Res*., 1993, **8**, 27.
5 P. Li, I. W. Chen and J. E. Penner-Hahn, *Phys. Rev*., 1993, **48**, 10063.
6 J. D. McCullough and K. N. Trueblood, *Acta Crystallogr*., 1959, **12**, 507.
7 K. S. Mazdiyasni, C. T. Lynch and J. S. Smith, *J. Am. Ceram. Soc*., 1966, **49**, 286.
8 G. Katz, *J. Am. Ceram. Soc*., 1971, **54**, 531.
9 R. C. Garvie, *J. Phys. Chem*., 1965, **69**, 1238.
10 B. H. Davis, *J. Am. Ceram. Soc*., 1984, **67**, 168.
11 G. Gimblett, A. A. Rahman and K. S. W. Sing, *J. Chem. Tech. Biotechnol*., 1980, **30**, 51.
12 R. A. Comelli, C. R. Vera and J. M. Parera, *J. Catal*., 1995, **151**, 96.
13 T. K. Gupta, J. H. Bechtold, R. C. Kurnichi, L. H. Gadoff and B. R. Rossing, *J. Mater. Sci*., 1977, **12**, 2421.
14 T. K. Gupta, F. F. Lange and J. H. Bechtold, *J. Am. Chem. Soc*., 1978, **13**, 1464.
15 R. C. Garvie, R. H. Hnnink and R. T. Pascoe, *Nature* (*London*), 1975, **258**, 703.
16 A. G. Evans, *Adv. Ceram*., 1984, **12**, 193.
17 E. C. Subarrao, *Ferroelectrics*, 1990, **102**, 267.
18 A. Chatterjee, S. K. Pradhan, A. Datta, M. Deand and D. Chakraverty, *J. Mater. Res*., 1994, **9**, 263.
19 R. C. Garvie, *J. Mater. Sci*., 1985, **20**, 3479.
20 M. G. Blanchin, G. Nihoul and E. Bernstein, *Philos. Mag*., 1992, **65**, 683.
21 M. Vallet-Regí, V. Ragel, J. Román, J. L. Martínez, M. Labeau and J. M. González-Calbet, *J. Mater. Res*., 1993, **8**, 138.
22 S. Hovmöller, *Ultramicroscopy*, 1992, **41**, 121.
23 S. H. R. Zhu and J. M. Zuo, EMLab Software, version 1, 1995.
24 R. C. Garvie and P. S. Nicholson, *J. Am. Ceram. Soc*., 1972, **55**, 303.
25 W. N. Schreiner and R. Jenkins, *Adv. X-Ray Anal*., 1983, **26**, 141.
26 *P.C-APD software, user's guide*, Philips Electronics N. V., 1st edn., 1993.
27 H. P. Klug and L. E. Alexander, in *XRD Diffraction procedures for polycrystallines and amorphous materials*, Wiley and Sons, 1974.
28 G. van Tendeloo, L. Anders and G. Thomas, *Acta Metall*., 1983, **31**, 1619.
29 R. Srinivasan, B. H. Davis, L. A. Rice and R. De Angelis, *J. Mater. Sci*., 1992, **27**, 661.
30 T. Mitsuhashi, M. Ichihara and T. Tatsuke, *J. Am. Ceram. Soc*., 1974, **57**, 91.
31 J. E. Bailey, *Proc. R. Soc. London, Ser. A*, 1964, **27**, 9395.
32 G. H. Bansal and A. H. Heuer, *Acta Metall*., 1972, **20**, 1281.
33 G. H. Bansal and A. H. Heuer, *Acta Metall*., 1974, **22**, 409.
34 L. A. Bursill, A. Pring, D. J. Smith and M. D. Shannon, *Philos. Mag. A*, 1982, **45**, 771.
35 K. Aizu, *Phys. Rev. B*, 1970, **2**, 754.
36 D. V. Dyck, G. V. Tendeloo and S. Amenlickx, *Ultramicroscopy*, 1984, **15**, 357.

Paper 6/07797H; *Received* 18*th November*, 1996